

Infrared 2–4 Micron Spectroscopy and Millimeter Interferometric HCN and HCO⁺ Observations of the Individual Merging Components of Arp299

Masatoshi Imanishi

*National Astronomical Observatory, 2-21-1, Osawa, Mitaka, Tokyo 181-8588, Japan
masa.imanishi@nao.ac.jp*

and

Kouichiro Nakanishi

*Nobeyama Radio Observatory, Minamimaki, Minamisaku, Nagano, 384-1305, Japan
nakanisi@nro.nao.ac.jp*

(Received 2006 June 7; accepted 2006 August 14)

Abstract

We present ground-based infrared K - (2–2.5 μm) and L -band (2.8–4.1 μm) spectroscopy, as well as interferometric observations at $\lambda \sim 3\text{mm}$, for the individual merging components (A, B, and C) of the luminous infrared galaxy Arp 299. We investigate the presence and location of the putative buried active galactic nucleus (AGN) inferred from previous X-ray observations at $E > 10\text{ keV}$. Our sub-arcsec-resolution infrared spectra clearly reveal that the putative buried AGN resides in the nucleus B1 (a subcomponent of B), based on a very low equivalent width of 3.3 μm polycyclic aromatic hydrocarbon emission, a weak 2.3 μm CO absorption feature, and a large time variation of the K - and L -band continuum fluxes. In component C, we find strong 3.1 μm ice absorption at L and weak 2.3 μm CO absorption at K , as expected in a buried AGN; however, a centrally concentrated young super star cluster is an alternative possibility because of the modest infrared luminosity and non-galaxy-nucleus nature of this component. The infrared K - and L -band spectra of the infrared brightest nucleus, A, are typical of a normal starburst with no explicit AGN signatures. Our interferometric observations simultaneously obtain HCN ($J = 1-0$) and HCO⁺ ($J = 1-0$) emission lines with ~ 4 arcsec resolution, and we find the HCN to HCO⁺ brightness-temperature ratios to be as low as those found in starburst nuclei in all the major merging components of Arp 299. The low ratio even in the AGN-hosting nucleus B may be due to the presence of a large amount of high-density molecular gas whose chemistry is dominated by coexisting starbursts and/or shocks, rather than by the central strong X-ray-emitting AGN.

Key words: galaxies: active — galaxies: nuclei — galaxies: ISM — radio lines: galaxies — infrared: galaxies — galaxies: individual (Arp299)

1. Introduction

Luminous infrared galaxies (LIRGs; $L_{\text{IR}} \gtrsim 10^{11} L_{\odot}$), discovered by the *IRAS* all sky survey, radiate the bulk of their luminosities as dust emission in the infrared (Sanders & Mirabel 1996). Powerful energy sources, starbursts and/or active galactic nuclei (AGNs), must therefore be present, but hidden behind dust. Since these LIRGs dominate the cosmic infrared background emission, which is the sum of dust-obscured activity in the universe (Dole et al. 2006), distinguishing their energy sources is closely related to clarifying the connections between obscured AGN and starbursts.

The difficulty in disentangling an AGN from a starburst as the primary energy source of a LIRG comes from the fact that highly concentrated molecular gas and dust in a LIRG's nucleus (Sanders & Mirabel 1996) can easily *bury* an AGN in all directions. A luminous AGN surrounded by torus-shaped dust is distinguishable from a normal starburst galaxy relatively easily through op-

tical and infrared high-resolution spectroscopy (Veilleux & Osterbrock 1987; Genzel et al. 1998) because emission from the so-called narrow line regions (NLRs), which are well developed along the torus axis above a torus scale height and are photoionized by the central AGN's radiation, is visible from all directions (Antonucci 1993). However, the presence of a *buried* AGN in a LIRG's core is difficult to unveil with this conventional type of spectroscopy because no significant NLRs are expected to develop.

Even if a luminous buried AGN is present in a LIRG's core, starbursts are likely to coexist, surrounding the central AGN. When such a starburst/buried-AGN composite LIRG is observed at wavelengths of large dust extinction, the observed flux is dominated by the less obscured starbursts, with a small contribution from the more highly obscured buried AGN. It is therefore essential to observe at wavelengths of low dust extinction if we are to properly investigate the presence of a buried AGN in a LIRG's core. Several useful methods for this purpose currently ex-

ist. The first is to observe in the hard X-ray band at $E > 2$ keV. Since an AGN is intrinsically a much stronger X-ray emitter than a starburst (Elvis et al. 1994; Ranalli et al. 2003), the detection of strong but highly-absorbed X-ray emission can provide evidence of a luminous buried AGN in a LIRG’s core. The second is millimeter interferometric searches for the chemical effects of the strong X-ray-emitting AGN on the surrounding interstellar medium. Around a buried AGN, X-ray dissociation regions (XDRs; Maloney et al. 1996) should develop, rather than the photodissociation regions (PDRs) usually found in starburst regions. Since the emission mechanism is different, XDRs and PDRs can be distinguished if they show different flux ratios of emission lines. The feasibility of carrying out this distinction has been demonstrated using HCN ($J = 1-0$) ($\lambda = 3.3848$ mm) and HCO^+ ($J = 1-0$) ($\lambda = 3.3637$ mm) emission lines in the millimeter wavelength range (Kohno 2005). The third method is infrared spectroscopy. While a normal starburst should always show large-equivalent-width polycyclic aromatic hydrocarbon (PAH) emission features in the spectra at $\lambda_{\text{rest}} = 3-25$ μm in the rest-frame, an AGN displays a PAH-free continuum (Genzel et al. 1998; Imanishi & Dudley 2000). Infrared K -band (2.0–2.5 μm) spectroscopy can also be used to separate starburst and AGN emission, because a normal starburst displays CO absorption features at $\lambda_{\text{rest}} = 2.3-2.4$ μm , whereas an AGN does not (Ivanov et al. 2000; Imanishi & Alonso-Herrero 2004). Since a buried AGN is generally more difficult to find with any method than the surrounding less obscured starbursts, using a combination of these potentially powerful approaches can increase the likelihood of detecting the elusive buried AGN and help to draw a quantitatively consistent picture about the energetic importance of the buried AGN.

Arp 299 ($z = 0.010$) is a nearby well studied LIRG. It consists of three main merging components, the eastern component IC 694 (Arp 299 A) and the western components making up NGC 3690 (Arp 299 B and C) (Gehrz et al. 1983; Wynn-Williams et al. 1991). The Arp 299 B nucleus is divided into subcomponents (B1 and B2) with a separation of ~ 2.5 arcsec in the infrared (Wynn-Williams et al. 1991; Zhou et al. 1993; Miles et al. 1996; Keto et al. 1997; Lai et al. 1999; Soifer et al. 2001). The Arp 299 C region is taken to be a “non-nucleus” (Dudley & Wynn-Williams 1993; Charmandaris et al. 2002) and consists of the C and C’ components with a separation of ~ 5 arcsec in the infrared (Zhou et al. 1993; Miles et al. 1996; Keto et al. 1997; Lai et al. 1999; Soifer et al. 2001). A component D is detected in the radio at 6 cm (5 GHz) (Neff et al. 2004), but is not found in the deepest infrared image (Soifer et al. 2001). The whole merging system has an infrared luminosity of $L_{\text{IR}} \sim 5 \times 10^{11} L_{\odot}$ ($= 10^{45.3}$ ergs s^{-1} ; see Table 1), approximately 60% of which comes from the A (IC 694) nucleus, based on observations using the *Kuiper Airborne Observatory* (Joy et al. 1989; Charmandaris et al. 2002). Although no explicit AGN signatures have been found in any nucleus through optical spectroscopy (Bushouse & Gallagher 1984; Keel et al. 1985; Armus et al. 1989; Coziol et al. 1998), highly-absorbed (Compton-thick; $N_{\text{H}} > 10^{24}$

cm^{-2}) but intrinsically strong X-ray emission has been detected at $E > 10$ keV (Della Ceca et al. 2002), suggesting the presence of a luminous buried AGN. Unfortunately, because of the lack of spatial resolution of the X-ray data at $E > 10$ keV, it is unclear which nucleus (or nuclei) possesses the buried AGN. While the equivalent width of the 6.4-keV iron $K\alpha$ line ($\text{EW}_{K\alpha}$) in higher spatial-resolution X-ray data at $E < 10$ keV was used to argue that a putative AGN resides in nucleus B1, at least (Zezas et al. 2003; Ballo et al. 2004), it is unclear whether an AGN is present in any of the other nuclei because the 6.4-keV emission can be weak in a Compton-thick *buried* AGN (Fabian et al. 2002). Further observational data are required to better understand the role of the putative buried AGN in Arp 299.

To spatially separate the subcomponents of the Arp 299 merging system, observations with spatial resolution better than a few to 5 arcsec are desirable. Ground-based infrared K - (2.0–2.5 μm) and L -band (2.8–4.1 μm) spectroscopy using a large ($> 3\text{m}$) telescope at a good observing site can achieve sub-arcsec spatial resolution and so is suitable for this purpose. At millimeter wavelengths, interferometry is better suited than a single-dish radio telescope to obtain morphological information, by resolving the subcomponents, and to investigate the properties of molecular gas at nuclear regions where AGNs are thought to exist, by reducing the contamination from extended emission. In this paper, we report on the results of sub-arcsec-resolution infrared K - and L -band spectroscopy and millimeter interferometric maps with ~ 4 arcsec resolution, of the HCN ($J = 1-0$) and HCO^+ ($J = 1-0$) emission lines for the individual main merging components of Arp 299. The aim is to identify the location(s) of the putative buried AGN. Throughout this paper, $H_0 = 75$ $\text{km s}^{-1} \text{Mpc}^{-1}$, $\Omega_{\text{M}} = 0.3$, and $\Omega_{\Lambda} = 0.7$ are adopted, so that the distance to Arp 299 is 40.3 Mpc and 1 arcsec corresponds to 190 pc.

2. Observations and Data Reduction

2.1. Infrared K - and L -band Spectroscopy

Infrared K - (2.0–2.5 μm) and L -band (2.8–4.1 μm) spectra of the Arp 299 A (IC 694), B and C were taken using SpeX (Rayner et al. 2003) attached to the IRTF 3-m telescope atop Mauna Kea, Hawaii, on 2005 April 27 (UT). The 1.9–4.2 μm cross-dispersed mode was employed, so that K - and L -band spectra were obtained simultaneously. For Arp 299, narrowband imaging data centered on the 3.3 μm PAH emission feature were available (Satyapal et al. 1999) and revealed that the 3.3- μm PAH emission is spatially extended, with a size of 2 to 3 arcsec. The imaging data can provide a rough absolute observed 3.3- μm PAH-emission luminosity and its ratio relative to the infrared luminosity (Satyapal et al. 1999). We therefore chose a relatively narrow $0''.8$ wide slit, to pinpoint the continuum emission peak of each merging component where the putative AGN may be located. Accordingly, the extended starburst emission is not fully covered with our infrared spectra. We search for

buried AGN signatures at the nucleus, based on the *equivalent width* of emission and absorption features in the *K*- and *L*-bands, since these equivalent width values cannot be obtained in detail from the narrowband imaging data (Satyapal et al. 1999). The resulting spectral resolution using this slit is $R \sim 1000$ in the *K*- and *L*-bands.

Observations of Arp 299 A, B (B1+B2), and C were performed independently. The position angle of the slit was set along the north–south direction for Arp 299 A and C, while for Arp 299 B it was 37° west-of-north to accommodate the signals from the B1 and B2 nuclei simultaneously (Zhou et al. 1993; Satyapal et al. 1999; Lai et al. 1999). Spectroscopy of Arp 299 C' was not attempted because its *K*- and *L*-band fluxes reported in the literature (Zhou et al. 1993) are more than 1 mag fainter than the other components, and thus it would be difficult to obtain a meaningful spectrum within the limited observing time available to us. The total net on-source integration times were 60, 60, and 30 min for components A, B (B1+B2), and C, respectively. The sky conditions were photometric throughout the observations. The seeing at *K* was measured to be in the range $0''.8$ – $1''.0$ in full-width at half-maximum (FWHM). A standard telescope nodding technique (ABBA pattern) with a throw of $7''.5$ was employed along the slit. The telescope tracking was monitored with the infrared slit-viewer of SpeX. Each exposure was 15 sec, and 2 coadds were made at each position.

The F8V main sequence star HR 4112 ($V = 4.84$) was observed as a standard star, with an airmass difference of <0.1 to the individual main merging components, to correct for the transmission of the Earth's atmosphere. The magnitude of the standard star HR 4112 was estimated to be $K = 3.49$ and $L = 3.45$, based on its *V*-band ($0.6 \mu\text{m}$) magnitude ($V = 4.84$) and the color of an F8V star ($V - K = 1.35$ and $V - L = 1.39$) (Tokunaga 2000). For reference, the *K*-band magnitude of HR 4112 in the 2MASS database (Skrutskie et al. 2006) is $K = 3.64 \pm 0.22$ mag, consistent with the above estimated value within the uncertainty. Standard data reduction procedures were employed using IRAF¹. Initially, bad pixels and pixels hit by cosmic rays were replaced with values interpolated from the surrounding pixels. Then, frames taken with an A (or B) beam were subtracted from frames subsequently taken with a B (or A) beam, and the resulting subtracted frames were added, then divided by a spectroscopic flat image. The spectral extraction of Arp 299 merging components along the slit was then made by integrating signals over $3''.0$ (0.15 arcsec pixel scale \times 20 pixels) because the emission is slightly spatially extended. For HR 4112, the actual image size along the slit tended to increase with decreasing wavelength, and was different for the different datasets taken at different times, due to changes in the seeing size. Thus, the pixel number used for the spectral extraction of HR 4112 varied, but was usually smaller than the value of $3''.0$ employed for Arp 299. Wavelength cal-

ibration was performed using the wavelength-dependent transmission of the Earth's atmosphere. The spectra of Arp 299's individual merging components were divided by that of the standard star HR 4112, and were multiplied by a blackbody spectrum with a temperature of 6000 K, corresponding to an F8V star (Tokunaga 2000). Appropriate spectral binning was applied to reduce scatter. Flux calibration was made using signals detected inside our slit spectra. Since the employed slit width was comparable to or slightly smaller than the seeing size, our slit spectra may have introduced a small amount of flux ambiguity even for the compact (spatially unresolved) emission at the peak of each merging component. However, this ambiguity is not expected to exceed several 10% greatly because of the confirmed tracking accuracy of IRTF SpeX. Hence, our slit spectra can provide a *rough* flux estimate for the compact emission.

2.2. Millimeter Interferometric Observations

Millimeter interferometric observations of HCN ($J = 1-0$) ($\lambda_{\text{rest}} = 3.3848$ mm or $\nu_{\text{rest}} = 88.632$ GHz in the rest-frame) and HCO⁺ ($J = 1-0$) ($\lambda_{\text{rest}} = 3.3637$ mm or $\nu_{\text{rest}} = 89.188$ GHz) lines were performed with the Nobeyama Millimeter Array (NMA) at Nobeyama Radio Observatory (NRO). The NMA consists of six 10-m antennas. NMA observations were performed in the D (with longest baseline of 82 m), C (163 m), and AB (351 m) configurations. The observing log is summarized in Table 2.

The backend was the Ultra-Wide-Band Correlator, UWBC (Okumura et al. 2000), which was configured to cover 1024 MHz with 128 channels at 8-MHz resolution. The central frequency was set to be 87.99 GHz, to cover the HCN and HCO⁺ lines simultaneously, redshifted to ~ 87.75 GHz and ~ 88.30 GHz, respectively. The bandwidth of 1024 MHz corresponds to ~ 3500 km s⁻¹ at $\nu \sim 88$ GHz. The field of view is ~ 77 arcsec at this frequency. Since the Hanning window function was applied to reduce side lobes in the spectra, the actual resolution was broadened to 16 MHz or 55 km s⁻¹ at $\nu \sim 88$ GHz. To calibrate the passband across the 128 channels, the bright quasar 0420–014 was observed at the beginning of each observing day. The quasar 1150+497 was used to calibrate temporal variations in the visibility amplitude and phase.

Standard data reduction was performed using the package UVPROC-II developed at NRO (Tsutsumi et al. 1997). For all the data, antenna baselines, band-pass properties, and time variations of the visibility amplitude and phase were corrected. Data taken during some parts of observing time showed large phase scatters, owing to bad radio seeing. These useless datasets were removed from our analysis. After clipping a small fraction of unusually high amplitude data, the data were Fourier-transformed using a natural *uv* weighting. The flux-calibration of Arp 299 was made by observing the quasar 1749+096, whose flux level relative to Uranus and Neptune had been measured. A conventional CLEAN method was applied to deconvolve the synthesized beam pattern. Since Arp 299 consists of distinct merging components and thus shows a spatially extended structure,

¹ IRAF is distributed by the National Optical Astronomy Observatories, operated by the Association of Universities for Research in Astronomy, Inc. (AURA), under cooperative agreement with the National Science Foundation.

the primary beam pattern of the NMA antenna was corrected. The total net on-source integration time of Arp 299 was ~ 25 h. The synthesized beam size was $4''.2 \times 3''.8$ (position angle is 26° west of north), and the absolute positional uncertainty of the NMA map is well below 1 arcsec.

3. Results

3.1. Infrared Spectra of Arp 299 A, B1, and C

Figures 1 and 2 present, respectively, the infrared L - and K -band spectra of Arp 299 A, B1, and C. Although Arp 299 B1 and B2 were simultaneously observed, and signals from both the nuclei were recognizable, B2 turned out to be much fainter than B1. In the literature, the nuclear flux of B1 has been reported to be only a factor of 5 and 1.6 brighter than B2 in the L - and K -bands, respectively, when measured with a 1–2-arcsec aperture (Zhou et al. 1993; Soifer et al. 2001). However, the contrast of the nuclear L - and K -band flux of B1, relative to B2, is nearly an order of magnitude in our spectra. Reliable spectral extraction of the much fainter B2 component was therefore very difficult. Although we do not show infrared L - and K -band spectra of B2 in this paper, it is less likely that a luminous buried AGN is present in B2 because the small B2 to B1 flux ratio at $10 \mu\text{m}$ (Soifer et al. 2001) suggests that dust emission heated by a putative buried AGN in B2 is weak, and the infrared K -band spectrum of B2 is typical of a starburst galaxy, with no explicit AGN signatures (Shier et al. 1996; Alonso-Herrero et al. 2000).

3.1.1. L -band spectra

The $3.3 \mu\text{m}$ PAH emission feature is detected clearly at the infrared continuum peaks of the A, B1, and C components (Figure 1), suggesting the presence of a large amount of starburst activity there. To estimate the $3.3 \mu\text{m}$ PAH strength, we adopt a template spectral shape for the Galactic star-forming regions and nearby starburst galaxies (type-1 sources; Tokunaga et al. 1991), as we have done previously for other LIRGs (Imanishi et al. 2006a; Imanishi 2006). The rest-frame $3.3 \mu\text{m}$ PAH emission equivalent widths we measured are summarized in column 2 of Table 3. Table 4 (column 2) tabulates the observed flux of the $3.3 \mu\text{m}$ PAH emission from the infrared continuum peaks. As noted in §2.1, unlike the equivalent width, the PAH *flux* can be subject to the effects of possible slit loss, even for spatially compact components, and so our flux estimates are only approximate.

The L -band spectrum of B1 displays an absorption feature at the longer wavelength side of the $3.3 \mu\text{m}$ PAH emission feature. We attribute this feature to $3.4 \mu\text{m}$ bare carbonaceous dust absorption, as seen in highly reddened Galactic stars (e.g., Pendleton et al. 1994; Imanishi et al. 1996; Rawlings et al. 2003) and obscured AGNs (e.g., Imanishi 2000a,b; Imanishi et al. 2001; Risaliti et al. 2003; Mason et al. 2004; Imanishi et al. 2006a). We estimate the optical depth of the $3.4 \mu\text{m}$ absorption feature to be $\tau_{3.4} \sim 0.06$, which corresponds to $A_V = 8\text{--}15$ mag, if the Galactic $\tau_{3.4}/A_V$ ratio is assumed ($= 0.004\text{--}0.007$; Pendleton et al. 1994).

A broad absorption feature at $\sim 3.1 \mu\text{m}$ is seen in the L -band spectrum of C. We ascribe this feature to $3.1 \mu\text{m}$ H_2O absorption, as observed in Galactic stars inside or behind molecular clouds (e.g., Smith et al. 1989, 1993; Murakawa et al. 2000) and LIRGs (Imanishi & Maloney 2003; Imanishi et al. 2006a; Imanishi 2006). The absorption optical depth is estimated to be $\tau_{3.1} \sim 1.4$.

3.1.2. K -band spectra

The K -band spectra in Figure 2 show emission lines of atomic and molecular (H_2) hydrogen in the Arp 299 A, B1, and C components. Table 5 summarizes the rest-frame equivalent widths of the H_2 S(1) ($\lambda_{\text{rest}} = 2.122 \mu\text{m}$) and $\text{Br}\gamma$ ($\lambda_{\text{rest}} = 2.166 \mu\text{m}$) emission lines, and their flux ratios, both of which are relatively insensitive to the possible slit loss.

The Arp 299 A spectrum shows a clear gap in the continuum at $\lambda_{\text{obs}} \sim 2.3 \mu\text{m}$ in the observed frame, which we attribute to CO absorption features at $\lambda_{\text{rest}} = 2.31\text{--}2.4 \mu\text{m}$ produced by stars (Ivanov et al. 2000; Imanishi & Alonso-Herrero 2004; Imanishi & Wada 2004). To estimate the CO absorption strengths in A, B1, and C, we adopt the spectroscopic CO index (CO_{spec}) defined by Doyon et al. (1994) and follow the procedures applied to other LIRGs (Imanishi et al. 2004; Imanishi 2006). Power-law continuum levels ($F_\lambda = \alpha \times \lambda^\beta$) are determined using data points at $\lambda_{\text{obs}} = 2.07\text{--}2.31 \mu\text{m}$ ($\lambda_{\text{rest}} = 2.05\text{--}2.29 \mu\text{m}$), excluding obvious emission lines. The adopted continuum levels are shown as dashed lines in Figure 2. Data at $\lambda_{\text{obs}} = 2.33\text{--}2.42 \mu\text{m}$ ($\lambda_{\text{rest}} = 2.31\text{--}2.40 \mu\text{m}$) are used to derive the CO_{spec} values. We obtain values of $\text{CO}_{\text{spec}} \sim 0.25$ (A), < 0.03 (B1), and ~ 0.1 (C).

3.2. Millimeter Interferometric Data

Aalto et al. (1997) and Casoli et al. (1999) have previously published millimeter interferometric maps of Arp 299 in the HCN ($J = 1\text{--}0$) line and nearby continuum; however, the HCO^+ ($J = 1\text{--}0$) line was not covered because of a relatively narrow frequency coverage. Ours are the first interferometric maps of Arp 299 in which the HCN and HCO^+ lines were simultaneously observed.

Spectra at the peak positions of A, B, C, and C' showed that the flux levels between the HCN ($J = 1\text{--}0$) and HCO^+ ($J = 1\text{--}0$) emission lines are substantially above the zero level, suggesting that continuum emission is present. We combined data points that were unaffected by the HCN and HCO^+ lines and made interferometric maps of the continuum emission at individual merging components. Figure 3 presents the contours of the continuum emission. The continuum emission is clearly detected in A, B (B1+B2), C, and C' and is slightly spatially extended, compared to the beam pattern, suggesting the presence of extended starbursts. A marginal indication of continuum emission exists, possibly associated with D in our map as well as in the map of Casoli et al. (1999), but its presence needs further confirmation. Although our millimeter interferometric data cannot resolve the B nucleus clearly into B1 and B2 with ~ 2.5 -arcsec separation (Wynn-Williams et al. 1991), most of the continuum emission appears to come from B1 (Figure 3). The estimated

~88 GHz continuum flux levels for each component are summarized in Table 6.

After subtracting the continuum, we investigate the spatial distribution of the HCN and HCO⁺ emission lines. Figures 4 and 5 show the integrated intensity map and channel map of the HCO⁺ and HCN emission lines, respectively. HCO⁺ emission is clearly detected in the A and B nuclei, and the C-C' region. Compared to the beam size, slight spatial extension is found in component A, but the HCO⁺ emission shows no major spatial extent in B. In the C region, the HCO⁺ emission is clearly spatially extended, and shows a peak between C and C', which we name C2. The HCN emission peaks at the A nucleus, where it is spatially unresolved. No clear HCN emission is found at B, C, or C' in our integrated intensity map, but some HCN emission may be present between C and C'.

Figure 6 shows continuum-subtracted spectra at the continuum peak positions of A, B, and C, and HCO⁺ peak C2. For B, C, and C2, flux excesses are seen at the expected HCN positions in the spectra, which we attribute to HCN emission. Figure 7 shows the Gaussian fits of the detected HCN and HCO⁺ emission lines at these peaks. The optical LSR velocity ($v_{\text{opt}} \equiv (\frac{\lambda}{\lambda_0} - 1) \times c$; c is the light speed) and FWHM of the emission lines are summarized in Table 7. The integrated fluxes of HCN and HCO⁺ at these peaks are derived from the Gaussian fits of the line profiles and are summarized in Table 8. For the spatially unresolved HCN emission from A and the HCO⁺ emission from B, the integrated fluxes are also estimated from the peak values of the contours of the integrated intensity maps in Figure 4. The estimated values are consistent with each other within 20%.

The HCN/HCO⁺ ratios in brightness temperature ($\propto \lambda^2 \times \text{flux density}$) at the A, B, C, and C2 peaks are also summarized in Table 8. Although the *absolute* flux levels of the NMA data are uncertain to within ~20%, this uncertainty does not propagate to the HCN/HCO⁺ *ratios* in brightness temperature because both lines were taken simultaneously with the same receiver and same correlator unit, under the same weather conditions, and were calibrated with the same procedure.

To take into account the flux of the extended components, we estimate the fluxes of HCO⁺ and HCN emission integrated over the area A, B, and C+C', based on the integrated intensity map in Figure 4. Table 9 tabulates the estimated values. For the HCN emission from A and HCO⁺ emission from B, the values from the integrated areas are similar to those for the peak positions, supporting the previous argument that the emission is spatially unresolved. However, for the HCO⁺ emission from A and C+C', the values are larger than those at the peaks, which is consistent with the presence of major spatially extended components, as was implied from the maps in Figure 4.

4. Discussion

4.1. Comparison to Previously Obtained Data

4.1.1. Infrared L-band spectra

The 3.3 μm PAH emission from Arp 299 has been detected previously by several groups (Mizutani et al. 1994; Dennefeld & Desert 1990; Satyapal et al. 1999; Imanishi & Dudley 2000). The equivalent widths of the 3.3 μm PAH emission ($\text{EW}_{3.3\text{PAH}}$) measured from these older data are tabulated in Table 3 and are compared to our data.

For the Arp 299 A nucleus, the $\text{EW}_{3.3\text{PAH}}$ values are similar for all the recently obtained data (this work; Satyapal et al. 1999; Imanishi & Dudley 2000). Older data presented by Dennefeld & Desert (1990) and Mizutani et al. (1994) show smaller values, which could be attributed to larger scatter and narrower wavelength coverage for their spectra compared to the more recent observations.

For Arp 299 C, the $\text{EW}_{3.3\text{PAH}}$ values reported here and by Mizutani et al. (1994) are a factor of 3 lower than that derived by Satyapal et al. (1999). This difference can naturally be explained by the strong 3.1 μm ice-covered dust absorption feature detected in our L-band spectrum. Because of the flux depression caused by this absorption feature, the actual continuum level is better derived from data at $\lambda > 3.4 \mu\text{m}$. The use of a data point at $\lambda = 3.159 \mu\text{m}$ (Satyapal et al. 1999) can lead to a major overestimate of the 3.3 μm PAH emission strength.

For Arp 299 B1, our $\text{EW}_{3.3\text{PAH}}$ value is substantially lower than those derived by Satyapal et al. (1999) and by Mizutani et al. (1994). Unlike Arp 299 C, no strong 3.1 μm absorption feature is detected in B1. We believe that this $\text{EW}_{3.3\text{PAH}}$ difference is likely to be caused by an increased continuum flux in our data compared to the older data, for the following reasons. First, the L-band continuum flux level is more than 1 mag brighter than the value from the literature (Zhou et al. 1993). Although our slit spectra have some flux ambiguity (§2.1), this difference in B1 is difficult to account for solely by this ambiguity because the L-band continuum flux levels for A and C are similar to those from the same study (Zhou et al. 1993). Next, the B1 and B2 nuclei were simultaneously observed in our spectra, and yet the L-band continuum level in B1 relative to B2 is more than 1 mag brighter than expected (Zhou et al. 1993). Unless the B2 flux has decreased substantially, a flux increase in B1 is strongly suggested.

In Table 4, the 3.3 μm PAH emission fluxes measured in previously obtained data are shown and compared with our data. We mainly use the highest quality recent data taken by Satyapal et al. (1999) for comparison with our data. In the A nucleus, both datasets provide similar fluxes. For the B nucleus, the bulk of the 3.3 μm PAH emission comes from B1 (Satyapal et al. 1999), and our estimate (B1) and that by Satyapal et al. (B1+B2) are similar to each other. In the C region, the PAH emission is extremely spatially extended (Satyapal et al. 1999), and the lower flux in our dataset can be explained by our smaller aperture, in addition to the above-mentioned PAH flux overestimate from their data. Overall, the compari-

son of PAH flux measurements suggests that our absolute flux calibration is reasonable, and thus the L -band continuum flux increase in B1 as implied above should be real.

4.1.2. Infrared K -band spectra

Some parts of the K -band spectra of the individual merging components of Arp 299 have been previously obtained (Nakagawa et al. 1989; Ridgway et al. 1994; Shier et al. 1994; Sugai et al. 1999; Alonso-Herrero et al. 2000). For the A and C components, the CO_{spec} values, as well as the emission properties of the H_2 S(1) and $\text{Br}\gamma$ (Table 5), are similar for our results and older spectra (Nakagawa et al. 1989; Ridgway et al. 1994; Shier et al. 1994; Sugai et al. 1999). For the B1 nucleus, however, the rest-frame equivalent widths of both H_2 S(1) and $\text{Br}\gamma$ emission lines in our data (Table 5) are a factor of ~ 3 smaller than those estimated from older data (Alonso-Herrero et al. 2000). Our estimate of $\text{CO}_{\text{spec}} (< 0.03)$ is also substantially lower than previous estimates (0.09–0.14; Ridgway et al. 1994; Alonso-Herrero et al. 2000). Finally, while the K -band continuum flux level for C is similar for our data and older spectra (Alonso-Herrero et al. 2000), that for B1 is brighter in our data. All of these results for B1 support the argument that the flux of the featureless K -band continuum has increased markedly and dilutes the emission and absorption features in the K -band spectrum of B1.

4.1.3. Millimeter interferometric data

For the continuum and HCN emission, our results can be compared to previously obtained interferometric maps (Aalto et al. 1997; Casoli et al. 1999) and to single-dish data (Solomon et al. 1992).

The continuum flux level was measured by Casoli et al. (1999) at $\nu = 87.7$ GHz to be 23.5 (A), 6 (B), 3 (C), and 4 mJy (C'). Our measurements at $\nu \sim 88$ GHz (Table 6) are similar to these for all components.

The HCN emission peaks at the A nucleus in our map, corroborating previous interferometric maps (Aalto et al. 1997; Casoli et al. 1999). The integrated HCN flux at the peak of the A nucleus (Table 8) and an integrated area surrounding it (Table 9) are similar within $\sim 30\%$ to the estimate by Aalto et al. (6.4 and 7 Jy km s^{-1} , respectively). In the map of Casoli et al. (1999), clear HCN emission is detected in B, C, and C', while it is not in our map. In the HCN integrated intensity map of Casoli et al. (1999), the noise level is lower than ours, and the highest contour at the B1 nucleus is 1.2 Jy $\text{km s}^{-1} \text{beam}^{-1}$, which is lower than the 3σ level of our map. For the HCN emission from C and C', the overall spatial distribution is similar for our maps and those of Casoli et al. (1999). In summary, the distribution of HCN emission from the whole Arp 299 merging system is consistent for all the available interferometric maps.

The linewidths are 310 km s^{-1} and 280 km s^{-1} in FWHM for HCN and HCO^+ emission, respectively, in the A nucleus. These values agree to within 20% with the ^{12}CO linewidth (350 km s^{-1} ; Aalto et al. 1997). In many LIRGs, the line profiles of HCN and ^{12}CO have been found to be similar (Gao & Solomon 2004; Imanishi et al.

2006b), and our data show this to be the case for the Arp 299 A nucleus. For the Arp 299 B and C components, the FWHM value is better determined from HCO^+ than HCN in our data because of the much higher S/N ratios in the former. The HCO^+ linewidths in FWHM are 230 km s^{-1} (B) and 130 km s^{-1} (C). For comparison, the ^{12}CO linewidths in FWHM are 260 km s^{-1} (B) and 60–80 km s^{-1} (C) (Aalto et al. 1997).

Finally, our new HCO^+ interferometric map, the first to be made for Arp 299, is compared to previous ^{12}CO maps (Sargent & Scoville 1991; Aalto et al. 1997; Casoli et al. 1999). At the A nucleus, an extended tail toward the southeast direction is recognizable in both HCO^+ and ^{12}CO maps. For the C' component, an extended HCO^+ emission component is detected on the eastern side of the C' peak, as was found in ^{12}CO and ^{13}CO maps (Sargent & Scoville 1991; Aalto et al. 1997; Casoli et al. 1999). However, while the ^{12}CO emission peaks at C and C', the HCO^+ emission, as well as the HCN emission (Casoli et al. 1999), has a peak between the C and C' components, suggesting that high-density ($n_{\text{H}_2} > 10^4 \text{ cm}^{-2}$) molecular gas, as probed by HCN and HCO^+ , is more concentrated in the in-between region than the diffuse ($n_{\text{H}_2} \sim 10^{2-3} \text{ cm}^{-2}$) gas probed by ^{12}CO .

4.2. The Location of the Buried AGN—Implications from Infrared Spectra

The infrared luminosity of Arp 299 is $2 \times 10^{45} \text{ ergs s}^{-1}$ (Table 1). The measured 3.3 μm PAH emission flux from the whole Arp 299 merging system (A+B+C) is $\sim 1.8 \times 10^{-12} \text{ ergs s}^{-1} \text{ cm}^{-2}$ (Satyapal et al. 1999), which corresponds to a 3.3 μm PAH luminosity of $3.5 \times 10^{41} \text{ ergs s}^{-1}$, with the caveat that the actual value is slightly smaller because of the overestimate in C (§4.1.1). If we adopt a 3.3 μm PAH to infrared luminosity ratio of $\sim 10^{-3}$, typical for starbursts (Mouri et al. 1990; Imanishi 2002), then the luminosity of detected starbursts becomes $3.5 \times 10^{44} \text{ ergs s}^{-1}$, which is a factor of 5 below the measured infrared luminosity. Although the extinction correction of the 3.3 μm PAH emission can increase the intrinsic starburst luminosity, the correction factor is only a factor of 2 to 3 for dust extinction with $A_V < 20$ mag measured in Arp 299 (Nakagawa et al. 1989; Satyapal et al. 1999; Alonso-Herrero et al. 2000), if the Galactic dust extinction curve is assumed (Rieke & Lebofsky 1985). Taken at face value, it is quite possible that AGN activity can play an important role energetically. In this section, we investigate in detail the nuclei containing buried AGN.

4.2.1. Arp 299 B1

The infrared L - and K -band spectra of the B1 nucleus favor the presence of a buried AGN there, based on the following three main arguments. First, the equivalent width of the 3.3 μm PAH emission in the L -band spectrum is only $\text{EW}_{3.3\text{PAH}} = 7 \text{ nm}$, more than an order of magnitude below typical values found in starburst galaxies ($\text{EW}_{3.3\text{PAH}} \sim 100 \text{ nm}$; Moorwood 1986; Imanishi & Dudley 2000). Second, the CO index in the K -band spectrum is $\text{CO}_{\text{spec}} < 0.03$, much lower than typical values found in starburst galaxies ($\text{CO}_{\text{spec}} > 0.15$; Goldader et

al. 1997a,b; Ivanov et al. 2000). A strong contribution from a featureless continuum, most likely originating from hot dust heated by an AGN, dilutes both the 3.3 μm PAH emission and 2.3 μm CO absorption features. Third, an increase in the *L*- and *K*-band continua is clearly recognizable, compared to old data taken about 5–10 years ago. Since no major flux variation is expected in a starburst over this time period, an AGN is the natural explanation. We conclude that the B1 nucleus contains a buried AGN, as was previously argued based on observations of 2–10 keV X-ray emission (Zezas et al. 2003; Ballo et al. 2004) and of the infrared 5–16 μm band (Gallais et al. 2004). Assuming a Galactic extinction curve of $\tau_{3.4}/A_V = 0.004$ – 0.007 (Pendleton et al. 1994; Imanishi et al. 1996) and $A_L \sim 0.06 \times A_V$ (Rieke & Lebofsky 1985), we can roughly estimate the dereddened luminosity of AGN-heated dust in the B1 nucleus from the observed *L*-band spectrum (optical depth of dust absorption features and observed continuum flux level at 3 to 4 μm) (Imanishi et al. 2001; Imanishi & Maloney 2003; Imanishi et al. 2006a), which is 3 – 5×10^{43} ergs s^{-1} .

4.2.2. Arp 299 C

Our infrared *L*-band spectrum of C displays a strong 3.1 μm ice absorption feature with $\tau_{3.1} \sim 1.4$. For a buried AGN in which the energy source is more centrally concentrated than dust, a foreground-screen dust-absorption geometry is applicable, while a mixed dust/source geometry is at work for a normal starburst in which stellar energy sources and dust are spatially well mixed (Puxley 1991; McLeod et al. 1993; Forster Schreiber et al. 2001). In a normal starburst with mixed dust/source geometry, whose radiation density, and therefore the fraction of dust covered with an ice mantle, is similar to the well studied starburst galaxy M82, the $\tau_{3.1}$ value is <0.3 for any amount of dust extinction of the starburst (Imanishi & Maloney 2003). Even if all dust is covered with an ice mantle ($f = 1$ in Imanishi & Maloney 2003), the mixed dust/source geometry can only provide a maximum of $\tau_{3.1} \sim 0.7$, assuming the dust properties are similar to the Galactic interstellar medium. This is because the observed flux is dominated by foreground, weakly obscured, less attenuated emission, with a small contribution from obscured, highly attenuated emission at the far side, in this mixed dust/source geometry. The large $\tau_{3.1}$ value in the Arp 299 C component (~ 1.4) would require a foreground-screen dust geometry. A centrally concentrated energy source, such as a buried AGN, may be present, in addition to a normal, PAH-emitting starburst (Figure 1). Alternatively, if a large amount of foreground-screen dust exists exterior to the normal starburst core (e.g., in an edge-on host galaxy), then the large $\tau_{3.1}$ can be explained. However, the $\text{EW}_{3.3\text{PAH}}$ value is ~ 40 nm in C. In this geometry, the $\text{EW}_{3.3\text{PAH}}$ value should have the value usually found for normal starbursts (~ 100 nm) because both PAH and continuum emission are attenuated in a similar manner. Dilution of the PAH emission by PAH-free continuum from an energy source other than a normal starburst is indicated from the *L*-band spectrum of C. In the C component, the observed CO_{spec} value

(~ 0.1) is also smaller than expected for a normal starburst (>0.15). Dilution by the featureless *K*-band continuum, possibly from AGN-heated hot dust or stars younger than $\sim 10^6$ yr (Leitherer et al. 1999), is required to explain this result.

Unlike the A and B nuclei, Arp 299 C+C' is thought to be a non-galaxy nucleus (Dudley & Wynn-Williams 1993; Charmandaris et al. 2002). Under the assumption of an Eddington mass accretion rate, a more massive black hole is necessary to produce a larger AGN luminosity, and supermassive black holes are generally present at galaxy nuclei. Whether the C component possesses a sufficiently large supermassive black hole for AGN activity is less clear than for the other Arp 299 nuclei. Alonso-Herrero et al. (2000) noticed a weaker CO absorption feature in the *K*-band spectrum of C, but attributed its weakness to the youth of the starbursts. If a very active super star cluster with an infrared luminosity of $L_{\text{IR}} \sim 10^9 L_{\odot}$ (Gorjian et al. 2001) is formed in the innermost regions of dense molecular gas and the radiation density there is so high as to destroy PAH molecules (Sellgren 1981), then a large $\tau_{3.1}$ value and PAH-free featureless *L*-band continuum (Alonso-Herrero et al. 2004) may be produced. For the nuclei of ultraluminous infrared galaxies with $L_{\text{IR}} > 10^{12} L_{\odot}$, energy sources that are more centrally concentrated than dust would require both large luminosity and high surface brightnesses, for which AGNs are the natural explanation (Soifer et al. 2000; Soifer et al. 2003). However, the infrared luminosity of Arp 299 C is at the level of $L_{\text{IR}} \sim 10^{10} L_{\odot}$ (Charmandaris et al. 2002). In Arp 299 C, the scenario of multiple young super star clusters embedded in dust and molecular gas may hold in term of absolute luminosity.

4.2.3. Arp 299 A

Among the merging components of Arp 299, the A nucleus (IC 694) has long been suggested to be the most probable AGN-harboring nucleus, based on near-infrared color (Nakagawa et al. 1989), compact high surface-brightness radio emission (Lonsdale et al. 1992; Lonsdale et al. 1993), and starburst modeling (Gehrz et al. 1983; Shier et al. 1996). However, our infrared *L*- and *K*-band spectra reveal no explicit AGN evidence in this nucleus: its $\text{EW}_{3.3\text{PAH}}$ and CO_{spec} values are typical of starburst galaxies (Moorwood 1986; Goldader et al. 1997a; Goldader et al. 1997b; Ivanov et al. 2000). Recent high-quality infrared data (Imanishi & Dudley 2000; Charmandaris et al. 2002; Gallais et al. 2004) have also failed to provide clear AGN signatures from A. Although Ballo et al. (2004) inferred the presence of an AGN in the A nucleus, based on the presence of 6.7 keV ionized iron emission, their argument is weaker than that based on the 6.4-keV iron $K\alpha$ line for the B1 nucleus. If a luminous buried AGN is present in the Arp 299 A nucleus, the AGN must be more elusive than in B1.

4.3. Interpretation of the HCN/HCO⁺ Ratios

Kohno et al. (2001) and Kohno (2005) proposed that AGN-dominated galaxy nuclei (XDRs) tend to show higher HCN ($J = 1-0$) to HCO⁺ ($J = 1-0$) and HCN

($J = 1-0$) to CO ($J = 1-0$) brightness-temperature ratios than starburst-dominated galaxy nuclei (PDRs), and thus that these ratios can be used to distinguish the two types of galaxies. In particular, both the HCN and HCO^+ molecules have similarly large dipole moments ($\mu \sim 3-4$ debye; Millar et al. 1997; Botschwina et al. 1993) and so probe similarly high-density ($n_{\text{H}_2} > 10^4 \text{ cm}^{-2}$) molecular gas. Hence, the HCN/ HCO^+ ratios are very useful for distinguishing between the two galaxy types, being unaffected by different dense-to-diffuse molecular gas fractions in different galaxies. Imanishi et al. (2004; 2006b) applied this method to a few LIRG nuclei, and successfully found high HCN/ HCO^+ brightness-temperature ratios in LIRGs known to possess luminous buried AGNs based on previously obtained data at other wavelengths. An HCN *abundance* enhancement in XDR chemistry of dense molecular gas around a strong X-ray illuminating source (Meijerink & Spaans 2005; their Fig.10, model 4) can naturally explain the high HCN/ HCO^+ brightness-temperature ratios in luminous AGNs, whether the HCN and HCO^+ emission is optically thin or thick (Imanishi et al. 2006b).

We use the HCN and HCO^+ flux measurements obtained with the NMA, to apply this energy diagnostic method to the individual merging components of Arp 299. For Arp 299, HCN and HCO^+ measurements using a single-dish radio telescope are available (Gracia-Carpio et al. 2006). However, our interferometric data have the following advantages over the single-dish measurements: Although single-dish radio data measure the HCN and HCO^+ emission from the combined B+C regions, our interferometric data can clearly resolve B and C because of better spatial resolution. In addition, we can probe the dense molecular gas for regions confined to the nuclei where putative AGNs are expected to reside, by reducing the contamination from extended starburst emission. The XDR volume can be large in a *pure* buried AGN with no starburst activity. However, in a starburst/buried-AGN composite galaxy, such as the majority of LIRGs, strong XDR signatures are expected only in the nuclear region in the close vicinity of a luminous X-ray-emitting AGN. Spatially extended molecular gas can be affected by the surrounding starbursts and thus show properties expected from PDRs. For the purpose of finding XDR signatures in starburst/AGN composite LIRGs, such as Arp 299, investigating the HCN/ HCO^+ ratios in regions confined to the nuclei, based on high-spatial-resolution interferometric data, is superior to using single-dish data. Furthermore, in the old single-dish data, HCN and HCO^+ observations were made at different times, whereas for our NMA interferometric data, the HCN and HCO^+ lines were simultaneously obtained, so that possible uncertainties due to time-variable observing conditions and inter-calibration are minimized, making the discussions of the HCN/ HCO^+ brightness-temperature *ratios* reliable.

Figure 8 shows the HCN ($J = 1-0$) to CO ($J = 1-0$) (abscissa) and HCN ($J = 1-0$) to HCO^+ ($J = 1-0$) (ordinate) ratios in brightness temperature of Arp 299 and other galaxies. For the Arp 299 merging components, the HCN/ HCO^+ brightness-temperature ratios are directly

derived from our NMA data, while the HCN/CO ratios are taken from the older interferometric data of Casoli et al. (1999). The Arp 299 A, B, and C components show low HCN/ HCO^+ brightness-temperature ratios, as observed in starburst-dominated galaxy nuclei.

Table 10 summarizes the detection or non-detection of AGN signatures based on various methods. Since a luminous buried AGN is almost certainly present in the B1 nucleus, we must consider why no XDR signature is found in B based on the HCN/ HCO^+ ratio. Several explanations are possible, but whichever scenario is correct, we have to conclude that the HCN/ HCO^+ method may miss some types of buried AGN despite their detection at other wavelengths.

First, the dereddened AGN luminosity at the B1 nucleus derived from our infrared L -band spectrum is $L_{\text{IR}}(\text{AGN}) \sim 3-5 \times 10^{43} \text{ ergs s}^{-1}$ (§4.2.1). The absorption-corrected 2–10 keV X-ray luminosity is $\sim 5 \times 10^{42} \text{ ergs s}^{-1}$ (Della Ceca et al. 2002). If we apply 2–10 keV to the bolometric luminosity correction of $\sim 10-20$ (Elvis et al. 1994), the estimated AGN luminosity becomes roughly similar, within a factor of 2–3, to the value quoted above based on our infrared L -band spectrum. However, the detected starburst luminosity in the B1 nucleus is estimated to be $L_{\text{IR}}(\text{SB}) \sim 4-5 \times 10^{43} \text{ ergs s}^{-1}$ based on the observed $3.3 \mu\text{m}$ PAH emission luminosity (This work; Satyapal et al. 1999) and on the ratio of $L_{3.3\text{PAH}}/L_{\text{IR}} \sim 10^{-3}$ found in starbursts (Mouri et al. 1990; Imanishi 2002). If we assume dust extinction of $A_V = 6-15 \text{ mag}$ for the detected starbursts in B (Gehrz et al. 1983; Beck et al. 1986; Satyapal et al. 1999), the extinction-corrected starburst luminosity can increase to $L_{\text{IR}}(\text{SB}) \sim 7-10 \times 10^{43} \text{ ergs s}^{-1}$. Thus, in the B nucleus, the starburst luminosity is comparable to the AGN luminosity. The presence of high-density molecular gas strongly affected by this luminous starburst component may hide the signatures of XDRs traced by our HCN/ HCO^+ method.

Second, for the HCN/ HCO^+ method to work in finding XDR signatures, the high-density molecular gas, as probed by HCN and HCO^+ , must be sufficiently close to be affected by the central AGN's X-ray radiation. In the double nuclei merging LIRG NGC 6240, the HCN and HCO^+ emission peaks are not at individual nuclei, but in the internuclear region where shocks are important (Nakanishi et al. 2005). In Arp 299, although the HCO^+ emission peak from B (B1+B2) appears to coincide with the B1 nucleus in our interferometric map with $4.''2 \times 3.''8$ spatial resolution (Figure 4), it is possible that the actual distribution is slightly displaced from the exact position of the B1 nucleus to the B2 side, and shocks may play a major role. It is known that shock regions show enhanced HCO^+ abundance (Dickinson et al. 1980), which can decrease the HCN/ HCO^+ brightness-temperature ratio, compared to a pure buried AGN. In fact, shocks driven by starburst superwinds are found to be prominent in the whole area of the Arp 299 merging system (Heckman et al. 1999). These spatially extended shocks at the surface of the buried AGN may decrease the HCN/ HCO^+ brightness-temperature ratio measured toward the B1 nu-

cleus.

Third, an increase in AGN luminosity compared to older data is indicated in our infrared spectra of B1 (§4.2.1). Some time lag may perhaps occur between the onset of an active AGN phase and the stage when the X-ray-emitting AGN can chemically affect the surrounding high-density molecular gas. If the very active AGN phase has just started, then the low HCN/HCO⁺ brightness-temperature ratio may be explained if the surrounding molecular gas has not been subjected to sufficient chemical effects.

Finally, the HCN/HCO⁺ abundance ratio is highly dependent on the density and distribution of molecular gas surrounding a central X-ray-emitting AGN (Meijerink & Spaans 2005). The Arp 299 merging components may have different molecular gas distributions (e.g., density and geometry) from other LIRGs for which our HCN/HCO⁺ method succeeded. Further detailed chemical calculations are needed to interpret more unambiguously the observed HCN/HCO⁺ brightness-temperature ratios in galaxies.

5. Summary

We performed infrared *L*- and *K*-band spectroscopy of the Arp 299 A, B1, and C regions to identify the location of the putative Compton-thick buried AGN, revealed by recent X-ray data. Emission and absorption features found in the *L*- and *K*-band spectra were used to distinguish between an AGN and a starburst. Millimeter interferometric maps of simultaneously taken HCN ($J = 1-0$) and HCO⁺ ($J = 1-0$) molecular lines were also presented for the Arp 299 A, B (B1+B2), and C regions. Using the interferometric maps, we determined the spatial distribution of these molecules and derived the HCN/HCO⁺ ratios in brightness temperature, to search for possible chemical signatures of the putative X-ray-emitting buried AGN to the surrounding interstellar medium. We obtained the following main conclusions.

1. Our infrared spectra strongly suggested that a luminous buried AGN is present in the B1 nucleus, based on a very low equivalent width of the 3.3 μm PAH emission in the *L*-band spectrum, a very weak 2.3 μm CO absorption feature in the *K*-band spectrum, and a major increase in the *L*- and *K*-band continuum fluxes compared to between 5 and 10 years ago. Our results supported previous arguments that the B1 nucleus hosts an AGN. The dereddened AGN luminosity from our infrared *L*-band spectrum was quantitatively comparable to that based on X-ray observations at $E > 10$ keV.
2. Our infrared spectra of the non-galaxy-nucleus Arp 299 C showed a large optical depth of 3.1 μm ice absorption ($\tau_{3.1} \sim 1.4$) in the *L* band, and a weak 2.3 μm CO absorption feature ($\text{CO}_{\text{spec}} \sim 0.1$) in the *K* band. Although a buried AGN is a plausible explanation, multiple young super star clusters are also a possibility, given the small infrared luminosity of Arp 299 C ($L_{\text{IR}} \sim 10^{10}L_{\odot}$).
3. In our infrared *L*- and *K*-band spectra of the A nucleus, we found no explicit evidence for an AGN.
4. Our millimeter interferometric maps confirmed that continuum emission is detected in the A, B, C, and C' regions and that HCN ($J = 1-0$) emission has a strong peak at the A nucleus. The flux and spatial distribution of the continuum and HCN emission were similar to those from previously obtained interferometric maps.
5. We presented the first interferometric map of Arp 299 in HCO⁺ ($J = 1-0$) line emission. HCO⁺ emission was clearly detected in the Arp 299 A, B, C, and C' regions. In the C and C' regions, the HCO⁺ emission peaks between these regions. This spatial distribution is similar to that of HCN, but is unlike the distribution of ¹²CO ($J = 1-0$), which shows peaks in the C and C' components. We conclude that high-density molecular gas, as probed by the HCN and HCO⁺ lines, has been swept to the in-between regions, while the more diffuse gas traced by ¹²CO has not.
6. We measured HCN/HCO⁺ ratios in brightness temperature for the A, B (B1+B2), and C regions, and compared the ratios with those of AGN- and starburst-dominated galaxies. The ratios in the three Arp 299 regions, even in the AGN-hosting B1 nucleus, were as low as seen in starburst-dominated galaxy nuclei, possibly because of the effects of co-existing starbursts and/or shocks.

We are grateful to the IRTF and NRO staff for their support during our observing runs. We thank S. Ishizuki for valuable discussions on the basics of interferometric observations of molecular gas. M.I. is supported by Grants-in-Aid for Scientific Research (16740117). M. I. is a visiting astronomer at the Infrared Telescope Facility, which is operated by the University of Hawaii under Cooperative Agreement no. NCC 5-538 with the National Aeronautics and Space Administration, Science Mission Directorate, Planetary Astronomy Program. NRO is a branch of the National Astronomical Observatory, National Institutes of Natural Sciences, Japan. Some parts of the data analysis were made using a computer system operated by the Astronomical Data Analysis Center (ADAC) and the Subaru Telescope of the National Astronomical Observatory. This publication makes use of data products from the Two Micron All Sky Survey, which is a joint project of the University of Massachusetts and the Infrared Processing and Analysis Center/California Institute of Technology, funded by the National Aeronautics and Space Administration and the National Science Foundation.

References

- Aalto, S., Radford, S. J. E., Scoville, N. Z., & Sargent, A. I. 1997, *ApJ*, 475, L107
- Alonso-Herrero, A., Rieke, G. H., Rieke, M. J., & Scoville, N. Z. 2000, *ApJ*, 532, 845
- Alonso-Herrero, A., Takagi, T., Baker, A. J., Rieke, G. H., Rieke, M. J., Imanishi, M., Scoville, N. Z. 2004, *ApJ*, 612, 222
- Antonucci, R. 1993, *ARA&A*, 31, 473
- Armus, L., Heckman, T. M., & Miley, G. K. 1989, *ApJ*, 347, 727
- Ballo, L., Braitto, V., Della Ceca, R., Maraschi, L., Tavecchio, F., & Dadina, M. 2004, *ApJ*, 600, 634
- Beck, S. C., Turner, J. L., & Ho, P. T. P. 1986, *ApJ*, 309, 70
- Botschwina, P., Horn, M., Flugge, J., Seeger, S. 1993, *J. Chem. Soc. Faraday Trans.*, 89, 2219
- Bushouse, H. A., & Gallagher, J. S., III. 1984, *PASP*, 96, 273
- Casoli, F., Willaime, M. -C., Viallefond, F., & Gerin, M. 1999, *A&A*, 346, 663
- Charmandaris, V., Stacey, G. J., & Gull, G., 2002, *ApJ*, 571, 282
- Coziol, R., Torres, C. A. O., Quast, G. R., Contini, T., & Davoust, E. 1998, *ApJS*, 119, 239
- Della Ceca, R. et al. 2002, *ApJ*, 581, L9
- Dennefeld, M., & Desert, F. X., 1990, *A&A*, 227, 379
- Dickinson, D. F., Rodriguez Kuiper, E. N., St. Clair Dinger, A., & Kuiper, T. B. H. 1980, *ApJ*, 237, L43
- Dole, H., et al. 2006, *A&A*, 451, 417
- Doyon, R., Joseph, R. D., & Wright, G. S. 1994, *ApJ*, 421, 101
- Dudley, C. C., & Wynn-Williams, C. G., 1993, *ApJ*, 407, L65
- Elvis, M., et al. 1994, *ApJS*, 95, 1
- Fabian, A. C., Wilman, R. J., & Crawford, C. S., 2002, *MNRAS*, 329, L18
- Forster Schreiber, N. M., Genzel, R., Lutz, D., Kunze, D., & Sternberg, A. 2001, *ApJ*, 552, 544
- Gallais, P., Charmandaris, V., Le Floc'h, E., Mirabel, I. F., Sauvage, M., Vigroux, L., & Laurent, O. 2004, *A&A*, 414, 845
- Gao, Y., & Solomon, P. M. 2004, *ApJS*, 152, 63
- Garcia-Marin, M. Colina, L., Arribas, S., & Alonso-Herrero, A. 2006, *ApJ*, in press (astro-ph/0606585)
- Gehrz, R. D., Sramek, R. A., & Weedman, D. W. 1983, *ApJ*, 267, 551
- Genzel, R. et al. 1998, *ApJ*, 498, 579
- Goldader, J. D., Joseph, R. D., Doyon, R., & Sanders, D. B. 1997a, *ApJ*, 474, 104
- Goldader, J. D., Joseph, R. D., Doyon, R., & Sanders, D. B. 1997b, *ApJS*, 108, 449
- Gorjian, V., Turner, J. L., & Beck, S. C. 2001, *ApJ*, 554, L29
- Gracia-Carpio, J., Garcia-Burillo, S., Planesas, P., & Colina, L. 2006, *ApJ*, 640, L135
- Heckman, T. M., Armus, L., Weaver, K. A., & Wang, J. 1999, *ApJ*, 517, 130
- Imanishi, M. 2000a, *MNRAS*, 313, 165
- Imanishi, M. 2000b, *MNRAS*, 319, 331
- Imanishi, M. 2002, *ApJ*, 569, 44
- Imanishi, M., 2006, *AJ*, 131, 2406
- Imanishi, M., & Alonso-Herrero, A. 2004, *ApJ*, 614, 122
- Imanishi, M., & Dudley, C. C. 2000, *ApJ*, 545, 701
- Imanishi, M., & Maloney, P. R. 2003, *ApJ*, 588, 165
- Imanishi, M., & Wada, K., 2004, *ApJ*, 617, 214
- Imanishi, M., Dudley, C. C., & Maloney, P. R. 2001, *ApJ*, 558, L93
- Imanishi, M., Dudley, C. C., & Maloney, P. R. 2006a, *ApJ*, 637, 114
- Imanishi, M., Nakanishi, K., & Kohno, K. 2006b, *AJ*, 131, 2888
- Imanishi, M., Nakanishi, K., Kuno, N., & Kohno, K. 2004, *AJ*, 128, 2037
- Imanishi, M., Sasaki, Y., Goto, M., Kobayashi, N., Nagata, T., & Jones, T. J. 1996, *AJ*, 112, 235
- Ivanov, V. D., Rieke, G. H., Groppi, C. E., Alonso-Herrero, A., Rieke, M. J., & Engelbracht, C. W. 2000, *ApJ*, 545, 190
- Joy, M., Lester, D. F., Harvey, P. M., Telesco, C. M., Decher, R., Rickard, L. J., & Bushouse, H. 1989, *ApJ*, 339, 100
- Keel, W. C., Kennicutt, R. C., Jr., Hummel, E., & van der Hulst, J. M. 1985, *AJ*, 90, 708
- Keto, E., et al. 1997, *ApJ*, 485, 598
- Kohno, K. 2005, in *AIP Conf. Ser.* 783, *The Evolution of Starbursts*, ed. S. Hüttemeister, E. Manthey, D. Bomans, & K. Weis (New York: AIP), 203 (astro-ph/0508420)
- Kohno, K., Matsushita, S., Vila-Vilaro, B., Okumura, S. K., Shibatsuka, T., Okiura, M., Ishizuki, S., Kawabe, R. 2001, in *ASP Conf. Ser.* 249, *The Central kpc of Starbursts and AGN*, ed. J. H. Knapen, J. E., Beckman, I. Shlosman, & T. J. Mahoney (San Francisco: ASP), 672 (astro-ph/0206398)
- Lai, O., Rouan, D., Rigaut, F., Doyon, R., & Lacombe, F. 1999, *A&A*, 351, 834
- Leitherer, C. et al. 1999, *ApJS*, 123, 3
- Lonsdale, C. J., Lonsdale, C., & Smith, H. E. 1992, *ApJ*, 391, 629
- Lonsdale, C. J., Smith, H. E., & Lonsdale, C. J. 1993, *ApJ*, 405, L9
- Maloney, P., Hollenbach, D., & Tielens, A. G. G. M. 1996, *ApJ*, 466, 561
- Mason, R. E., Wright, G., Pendleton, Y., Adamson, A. 2004, *ApJ*, 613, 770
- McLeod, K. K., Rieke, G. H., Rieke, M. J., & Kelly, D. M. 1993, *ApJ*, 412, 111
- Meijerink, R., & Spaans, M. 2005, *A&A*, 436, 397
- Miles, J. W., Houck, J. R., Hayward, T. L., & Ashby, M. L. N. 1996, *ApJ*, 465, 191
- Millar, T. J., Farquhar, P. R. A., & Willacy, K. 1997, *A&AS*, 121, 139
- Mizutani, K., Suto, H., & Maihara, T. 1994, *ApJ*, 421, 475
- Moorwood, A. F. M. 1986, *A&A*, 166, 4
- Mouri, H., Kawara, K., Taniguchi, Y., & Nishida, M. 1990, *ApJ*, 356, L39
- Murakawa, K., Tamura, M., & Nagata, T. 2000, *ApJS*, 128, 603
- Nakagawa, T., Nagata, T., Geballe, T. R., Okuda, H., Shibai, H., & Matsuhara, H. 1989, *ApJ*, 340, 729
- Nakanishi, K., Okumura, S., Kohno, K., Kawabe, R., & Nakagawa, T. 2005, *PASJ*, 57, 575
- Neff, S. G., Ulvestad, J. S., & Teng S. H., 2004, *ApJ*, 611, 186
- Okumura, S. et al. 2000, *PASJ*, 52, 393
- Pendleton, Y. J., Sandford, S. A., Allamandola, L. J., Tielens, A. G. G. M., & Sellgren, K. 1994, *ApJ*, 437, 683
- Puxley, P. J. 1991, *MNRAS*, 249, 11p
- Ranalli, P., Comastri, A., & Setti, G. 2003, *A&A*, 399, 39
- Rawlings, M. G., Adamson, A. J., & Whittet, D. C. B. 2003, *MNRAS*, 341, 1121
- Rayner, J. T., Toomey, D. W., Onaka, P. M., Denault, A. J., Stahlberger, W. E., Vacca, W. D., Cushing, M. C., & Wang, S. 2003, *PASP*, 115, 362
- Rieke, G. H., & Lebofsky, M. J. 1985, *ApJ*, 288, 618

- Ridgway, S. E., Wynn-Williams, C. G., & Becklin, E. E. 1994, ApJ, 428, 609
- Risaliti, G., et al. 2003, ApJ, 595, L17
- Sanders, D. B., & Mirabel, I. F. 1996, ARA&A, 34, 749
- Sargent, A., & Scoville, N. 1991, ApJ, 366, L1
- Satyapal, S. et al. 1999, ApJ, 516, 704
- Sellgren, K. 1981, ApJ, 245, 138
- Shier, L. M., Rieke, M. J., & Rieke, G. H. 1994, ApJ, 433, L9
- Shier, L. M., Rieke, M. J., & Rieke, G. H. 1996, ApJ, 470, 222
- Smith, R. G., Sellgren, K., & Tokunaga, A. T. 1989, ApJ, 344, 413
- Smith, R. G., Sellgren, K., & Brooke, T. Y. 1993, MNRAS, 263, 749
- Soifer, B. T. et al. 2000, AJ, 119, 509
- Soifer, B. T. et al. 2001, AJ, 122, 1213
- Soifer, B. T., Bock, J. J., Marsh, K., Neugebauer, G., Matthews, K., Egami, E., & Armus, L. 2003, AJ, 126, 143
- Solomon, P. M., Downes, D., & Radford, S. J. E. 1992, ApJ, 387, L55
- Skrutskie, M. F., et al. 2006, AJ, 131, 1163
- Sugai, H., Davies, R. I., Malkan, M. A., McLean, I. S., Usuda, T., & Ward, M. J. 1999, ApJ, 527, 778
- Tokunaga, A. T. 2000, in Allen's Astrophysical Quantities, ed. A. N. Cox (4th ed; Berlin: Springer), 143
- Tokunaga, A. T., Sellgren, K., Smith, R. G., Nagata, T., Sakata, A., & Nakada, Y. 1991, ApJ, 380, 452
- Tsutsumi, T. Morita, K. -I. & Umeyama, S. 1997, in Astronomical Data Analysis Software and Systems VI, ed. G. Hunt, & H. E. Payne (San Francisco: ASP), 50
- Veilleux, S., & Osterbrock, D. E. 1987, ApJS, 63, 295
- Wynn-Williams, C. G., Eales, S. A., Becklin, E. E., Hodapp, K. -W., Joseph, R. D., McLean, I. S., Simons, D. A., & Wright, G. S. 1991, ApJ, 377, 426
- Zezas, A., Ward, M. J., & Murray, S. S. 2003, ApJ, 594, L31
- Zhou, S., Wynn-Williams, C. G., & Sanders, D. B. 1993, ApJ, 409, 149

Table 1. Detailed information on Arp 299

Object	Redshift	f_{12} (Jy)	f_{25} (Jy)	f_{60} (Jy)	f_{100} (Jy)	$\log L_{\text{IR}}$ (ergs s $^{-1}$)	$\log L_{\text{IR}}/L_{\odot}$
(1)	(2)	(3)	(4)	(5)	(6)	(7)	(8)
Arp 299	0.010	3.8	23.2	103.7	107.4	45.3	11.7

Notes.

(1): Object.

(2): Redshift.

(3)–(6): f_{12} , f_{25} , f_{60} , and f_{100} are *IRAS FSC* fluxes at 12 μm , 25 μm , 60 μm , and 100 μm , respectively.

(7): Decimal logarithm of infrared (8–1000 μm) luminosity in ergs s $^{-1}$ calculated with $L_{\text{IR}} = 2.1 \times 10^{39} \times D(\text{Mpc})^2 \times (13.48 \times f_{12} + 5.16 \times f_{25} + 2.58 \times f_{60} + f_{100})$ ergs s $^{-1}$ (Sanders & Mirabel 1996).

(8): Decimal logarithm of infrared luminosity in units of solar luminosity.

Table 2. NMA observing log

Array Configuration	Observing Date (UT)
D	2004 Mar 12–14
C	2003 Dec 9
AB	2004 Jan 11

Table 3. Rest-frame equivalent width of the 3.3 μm PAH emission feature in [nm]

Component (1)	This work (2)	S99 (3)	DD90 (4)	M94 (5)	ID00 (6)
A	150 (0 $''$.8 \times 3 $''$.0)	130 ^a (2 $''$.7)	70 (2 $''$.7)	60 (5 $''$.4 \times 7 $''$.3)	150 (1 $''$.2 \times 10 $''$.0)
B1	7 (0 $''$.8 \times 3 $''$.0)	—	—	—	—
B (B1+B2)	—	14 ^a (7 $''$.1)	—	40 (5 $''$.4 \times 7 $''$.3)	—
C	40 (0 $''$.8 \times 3 $''$.0)	144 ^a (7 $''$.1)	—	40 (5 $''$.4 \times 7 $''$.3)	—

^a: Satyapal et al. (1999) performed narrowband imaging observations at 3.326 μm (PAH) and 3.159 μm (continuum). The flux level at 3.159 μm is taken as the representative continuum level at the wavelength of the 3.3 μm PAH emission feature.

Notes.

(1): Arp 299 merging component.

(2): This paper.

(3): Satyapal et al. (1999).

(4): Dennefeld & Desert (1990).

(5): Mizutani et al. (1994).

(6): Imanishi & Dudley (2000).

Table 4. 3.3 μm PAH emission flux in 10^{-16} [W m^{-2}]

Component (1)	This work (2)	S99 (3)	DD90 (4)	M94 (5)	ID00 (6)
A	4.5 ($0''.8 \times 3''.0$)	3.2 ($2''.7$)	5.0 ± 0.9 ($2''.7$)	5.8 ± 1.6 ($5''.4 \times 7''.3$)	6 ($1''.2 \times 10''.0$)
B1	2.0 ($0''.8 \times 3''.0$)	—	—	—	—
B (B1+B2)	—	2.7 ($7''.1$)	—	7.4 ± 1.5 ($5''.4 \times 7''.3$)	—
C	1.5 ($0''.8 \times 3''.0$)	6.3 ($7''.1$)	—	4.3 ± 1.5 ($5''.4 \times 7''.3$)	—

Notes.

(1): Arp 299 merging component.

(2): This paper.

(3): Satyapal et al. (1999).

(4): Dennefeld & Desert (1990).

(5): Mizutani et al. (1994).

(6): Imanishi & Dudley (2000).

Table 5. Br γ and H₂ S(1) emission lines

Component (1)	EW [nm]		EW [nm] (A00)		S(1)/Br γ (6)	S(1)/Br γ (S99) (7)
	H ₂ S(1) (2)	Br γ (3)	H ₂ S(1) (4)	Br γ (5)		
A	3	3	—	—	0.9	1.2
B1	0.3	0.3	1	0.9	1	—
C	<1.2	4	0.5	4	<0.3	0.12

Notes.

(1): Arp 299 merging component.

(2) and (3): Rest frame equivalent width of H₂ S(1) ($\lambda_{\text{rest}} = 2.122 \mu\text{m}$) and Br γ ($\lambda_{\text{rest}} = 2.166 \mu\text{m}$) emission lines in [nm], respectively, derived from our data.

(4) and (5): Rest frame equivalent width of H₂ S(1) and Br γ emission lines in [nm], respectively, derived by Alonso-Herrero et al. (2000).

(6): H₂ S(1) to Br γ flux ratio, derived from our data.

(7): H₂ S(1) to Br γ flux ratio, determined by Sugai et al. (1999).

Table 6. Continuum flux at the position of each merging component measured at $\nu \sim 88$ GHz

Component	Flux (mJy)
A	23.5 ± 1
B	6 ± 1
C	4.5 ± 1
C'	4.5 ± 1

Table 7. Gaussian fitting parameters of HCN and HCO⁺ emission lines

Component	LSR velocity (km s ⁻¹)		FWHM (km s ⁻¹)	
	HCN	HCO ⁺	HCN	HCO ⁺
(1)	(2)	(3)	(4)	(5)
A	3100	3100	310	280
B	3080	3150	100	230
C	3210	3170	160	130
C2	3220	3170	65	125

Notes.

(1): Arp 299 merging component.

(2): Optical LSR velocity $\{v_{\text{opt}} \equiv (\frac{\lambda}{\lambda_0} - 1) \times c\}$ of the HCN emission peak. For Arp 299, the LSR velocity is 5.9 km s⁻¹ larger than the heliocentric velocity. For B, C, and C2, the uncertainty may be large, because HCN emission is weak.

(3): Optical LSR velocity of the HCO⁺ emission peak.

(4): Line width of the HCN emission at FWHM. For B, C, and C2, the uncertainty may be large.

(5): Line width of the HCO⁺ emission at FWHM.

Table 8. Integrated intensity of HCN and HCO⁺ lines at the peak positions

Component	HCN (Jy km s ⁻¹)	HCO ⁺ (Jy km s ⁻¹)	HCN/HCO ⁺ (this work)	HCN/HCO ⁺ (single dish)
(1)	(2)	(3)	(4)	(5)
A	8.6	10.6	0.82	0.52
B	1.1	4.2	0.25	0.64 (B + C + C2)
C	1.5	3.2	0.47	
C2	0.56	2.0	0.28	

Notes.

(1): Arp 299 merging component.

(2): Integrated HCN intensity. For B, C, and C2, the uncertainty may be large.

(3): Integrated HCO⁺ intensity.

(4): HCN/HCO⁺ ratio in brightness temperature ($\propto \lambda^2 \times \text{flux density}$). The ratio is not affected by possible uncertainties in the absolute flux calibration.

(5): HCN/HCO⁺ ratio in brightness temperature, measured from single dish telescope's data (Gracia-Carpio et al. 2006).

Table 9. Fluxes of HCN and HCO⁺ lines, including spatially extended components

Component	HCN (Jy km s ⁻¹)	HCO ⁺ (Jy km s ⁻¹)
(1)	(2)	(3)
A	10	16
B	—	5
C+C'	3	12

Notes.

- (1): Arp 299 merging component.
(2): Integrated HCN intensity.
(3): Integrated HCO⁺ intensity.

Table 10. AGN signatures at individual major merging components of Arp 299, based on various methods

Method	A	B	C	Reference
(1)	(2)	(3)	(4)	(5)
Infrared <i>K</i> -band	X	○	△	a
Infrared <i>L</i> -band	X	○	△	a
HCN/HCO ⁺	X	X	X	a
Optical	X	X ^α	X	b,c,d,e
X-ray	△	○	X	f,g
Mid-infrared	X	○	X	h

α: Garcia-Marin et al. (2006) have recently argued the detection of AGN signatures through *integral field* optical spectroscopy.

Notes.

- (1): Methods.
(2)-(4): AGN signatures at Arp 299 A, B, and C components. ○: Strong. △: Possible. X: None.
(5): References for AGN signatures. (a): This work, (b): Bushouse & Gallagher (1984), (c): Keel et al. (1985), (d): Armus et al. (1989), (e): Coziol et al. (1998), (f): Zezas et al. (2003), (g): Ballo et al. (2004), (h): Gallais et al. (2004).

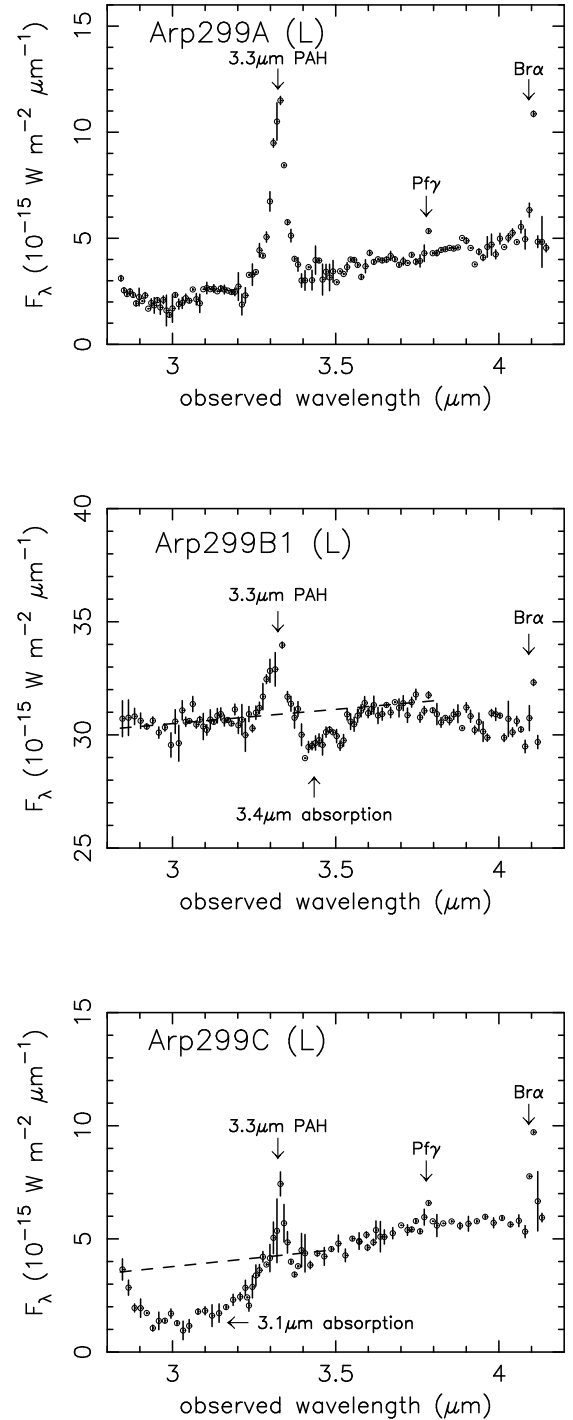


Fig. 1. Infrared *L*-band (2.8–4.1 μm) spectra of the Arp 299 A, B1, and C components. The abscissa and ordinate are the observed wavelength in μm and flux F_λ in $10^{-15} \text{ W m}^{-2} \mu\text{m}^{-1}$, respectively. The dashed lines in the Arp 299 B1 and C spectra are the adopted continuum levels, which were used to measure the optical depths of 3.4 μm bare carbonaceous dust (B1) or 3.1 μm ice-covered dust (C) absorption features, respectively. In addition to the detected 3.3 μm PAH emission, detected emission lines of hydrogen are indicated. Br α : Br α emission line at $\lambda_{\text{rest}} = 4.051 \mu\text{m}$. Pf γ : Pf γ emission line at $\lambda_{\text{rest}} = 3.738 \mu\text{m}$.

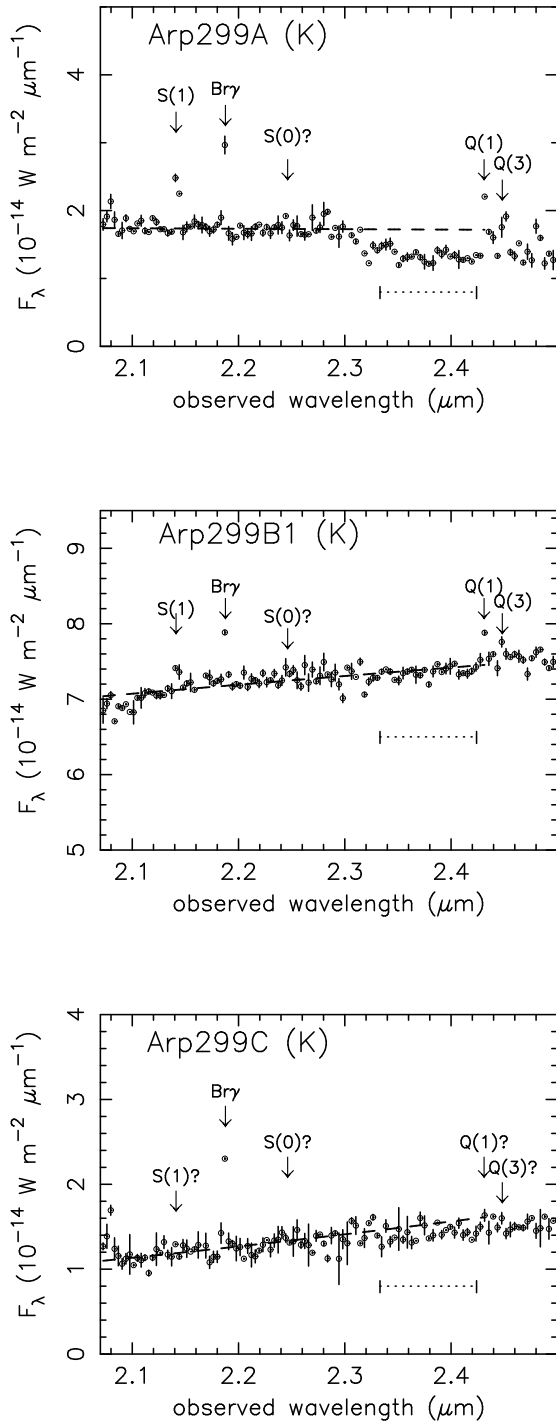


Fig. 2. Infrared K -band ($2.07\text{--}2.5\ \mu\text{m}$) spectra of the Arp 299 A, B1, and C components. The dotted lines inserted between the two vertical lines indicate the wavelength range of the CO absorption feature at $\lambda_{\text{rest}} = 2.31\text{--}2.40\ \mu\text{m}$ or $\lambda_{\text{obs}} = 2.33\text{--}2.42\ \mu\text{m}$. The dashed lines are the continuum levels adopted to measure the strengths of the CO absorption feature. Some detected emission lines are indicated. S(1): H_2 1–0 S(1) at $\lambda_{\text{rest}} = 2.122\ \mu\text{m}$. S(0): H_2 1–0 S(0) at $\lambda_{\text{rest}} = 2.223\ \mu\text{m}$. Q(1): H_2 1–0 Q(1) at $\lambda_{\text{rest}} = 2.407\ \mu\text{m}$. Q(3): H_2 1–0 Q(3) at $\lambda_{\text{rest}} = 2.424\ \mu\text{m}$. Br γ : Br γ emission line at $\lambda_{\text{rest}} = 2.166\ \mu\text{m}$.

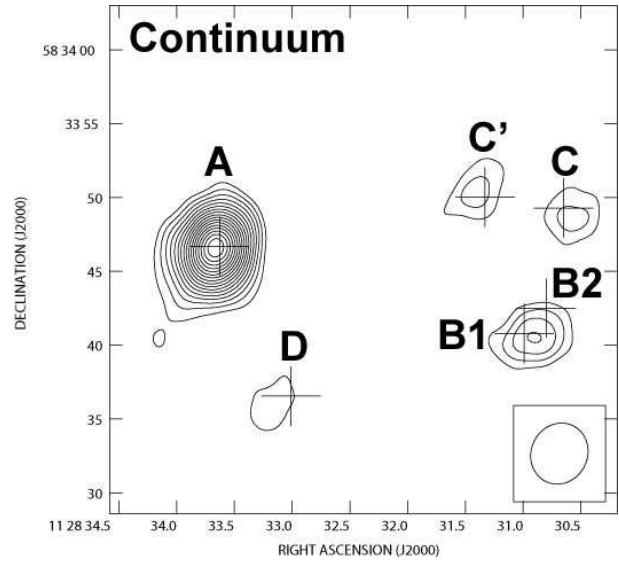


Fig. 3. Continuum emission map of Arp 299 at $\nu \sim 88\ \text{GHz}$. Contours start at $3\ \text{mJy beam}^{-1}$ and increase in steps of $1.2\ \text{mJy beam}^{-1}$. The location of the six main components, A, B1, B2, C, C', and D are indicated with large crosses. Their coordinates are taken from Neff et al. (2004).

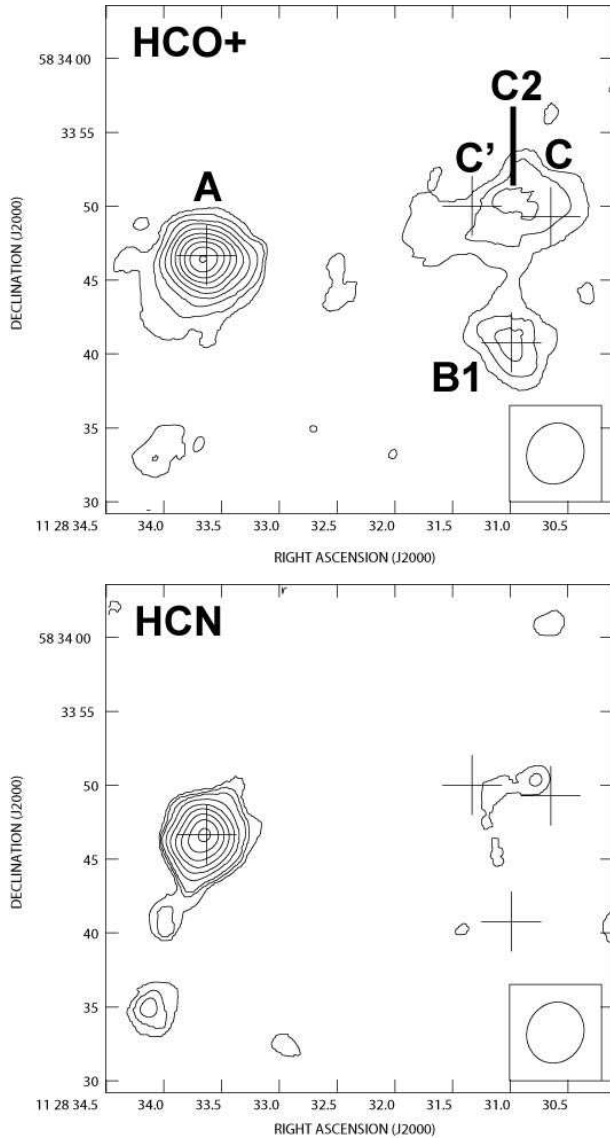


Fig. 4. *Left:* Integrated intensity map of HCO⁺ emission. The four major merging components (A, B1, C, C') are marked with large crosses. HCO⁺ emission is detected between C and C'. This region is named C2. Contours start at 1090 mJy beam⁻¹ km s⁻¹ and increase with 1090 mJy beam⁻¹ km s⁻¹ intervals. The r.m.s. noise level is ~545 mJy beam⁻¹ km s⁻¹. *Right:* Integrated intensity map of HCN emission. Four large crosses denote the location of A, B1, C, and C'. The lowest three contours are 2×, 3×, and 4× 545 mJy beam⁻¹ km s⁻¹, and then increase with 1090 mJy beam⁻¹ km s⁻¹. The r.m.s. noise level is ~545 mJy beam⁻¹ km s⁻¹.

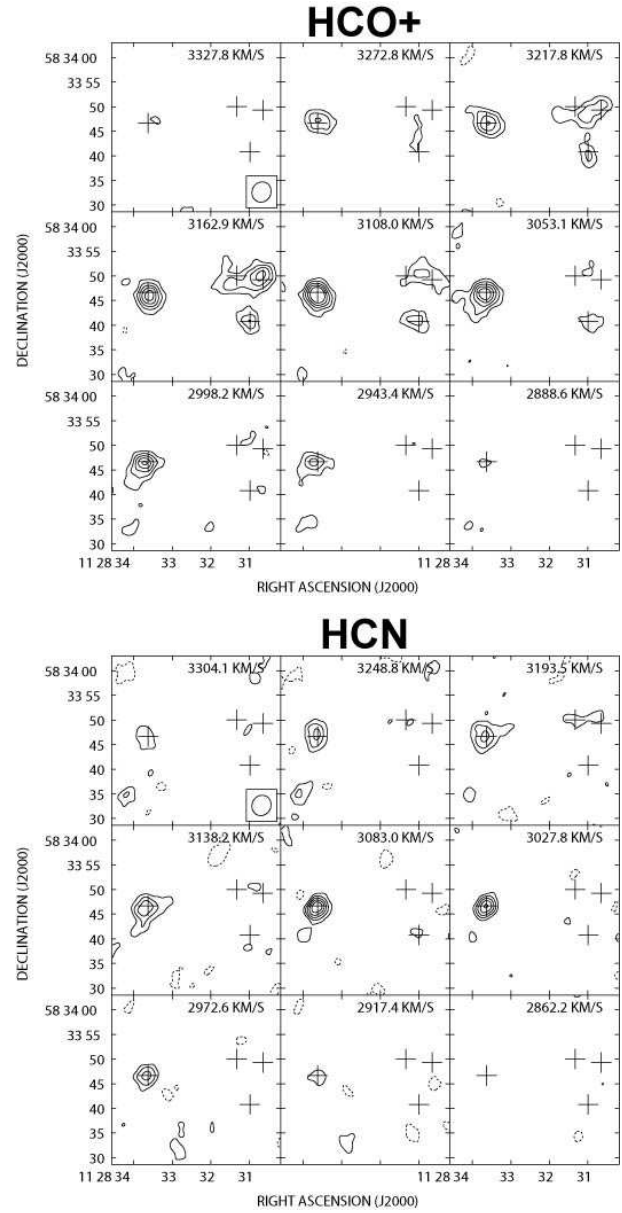


Fig. 5. *Left:* Channel map of HCO⁺ emission in units of optical LSR velocity $\{v_{opt} \equiv (\frac{\lambda}{\lambda_0} - 1) \times c\}$. Contours start at 7.5 mJy beam⁻¹, and increase with 5 mJy beam⁻¹ intervals. The r.m.s. noise level is ~2.5 mJy beam⁻¹. Positions of A, B1, C, and C' nuclei are plotted as crosses. *Right:* Channel map of HCN emission. Contours start at 7.5 mJy beam⁻¹, and increase with 5 mJy beam⁻¹ intervals. The r.m.s. noise level is ~2.5 mJy beam⁻¹.

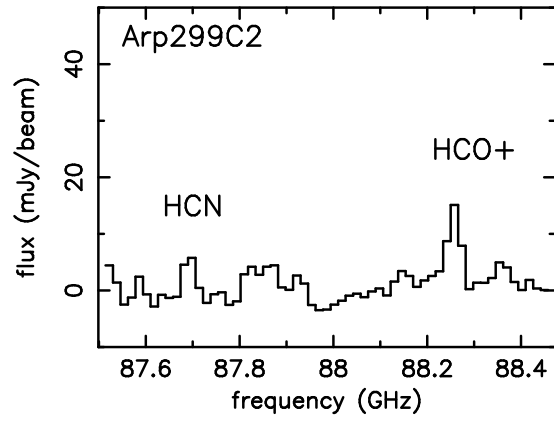
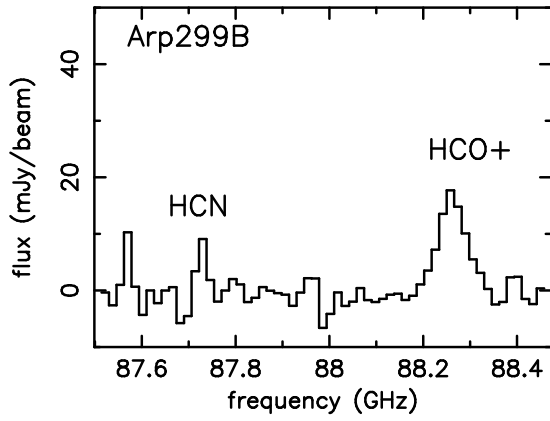
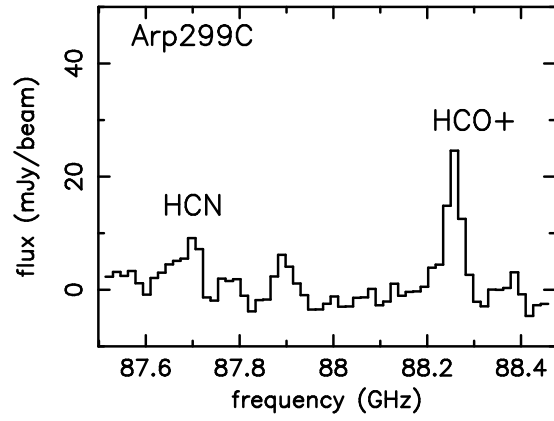
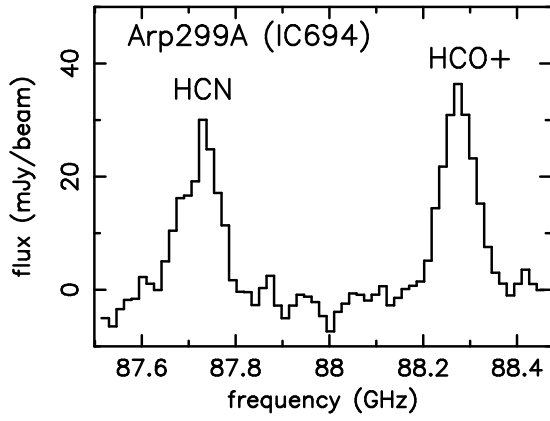


Fig. 6. Spectra at the peak positions of the components A, B, C, and C2. Peak positions are determined from our interferometric HCO⁺ data, not the coordinates provided by Neff et al. (2004).

Fig. 6. Continued

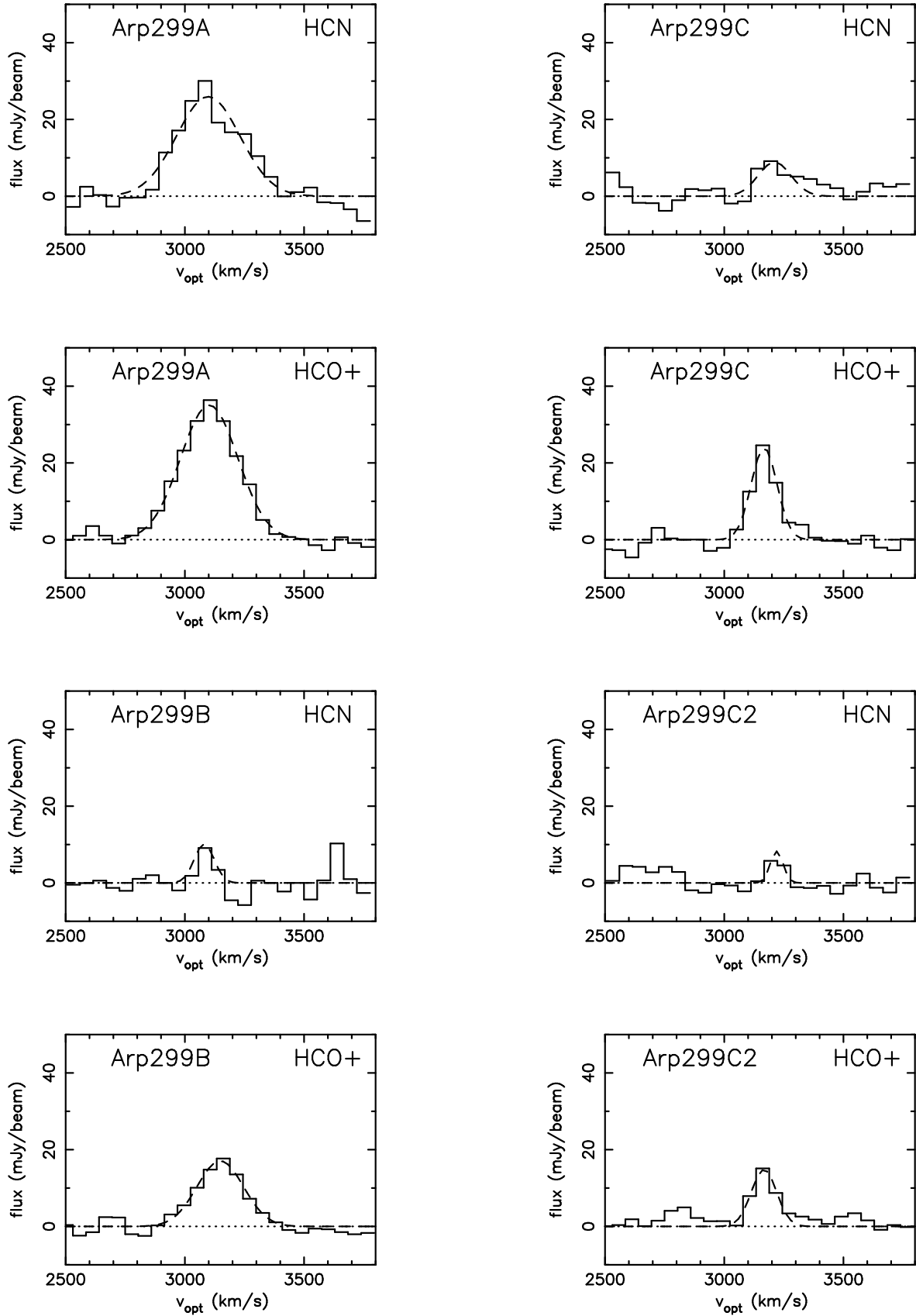


Fig. 7. Continued

Fig. 7. Gaussian fits to the HCN and HCO⁺ emission lines. The abscissa is the LSR velocity $\{v_{\text{opt}} \equiv (\frac{\lambda}{\lambda_0} - 1) \times c\}$ in km s⁻¹ and the ordinate is the flux in mJy beam⁻¹. Single Gaussian fits are used as defaults and are shown as dashed lines. Dotted lines denote the adopted continuum levels (=

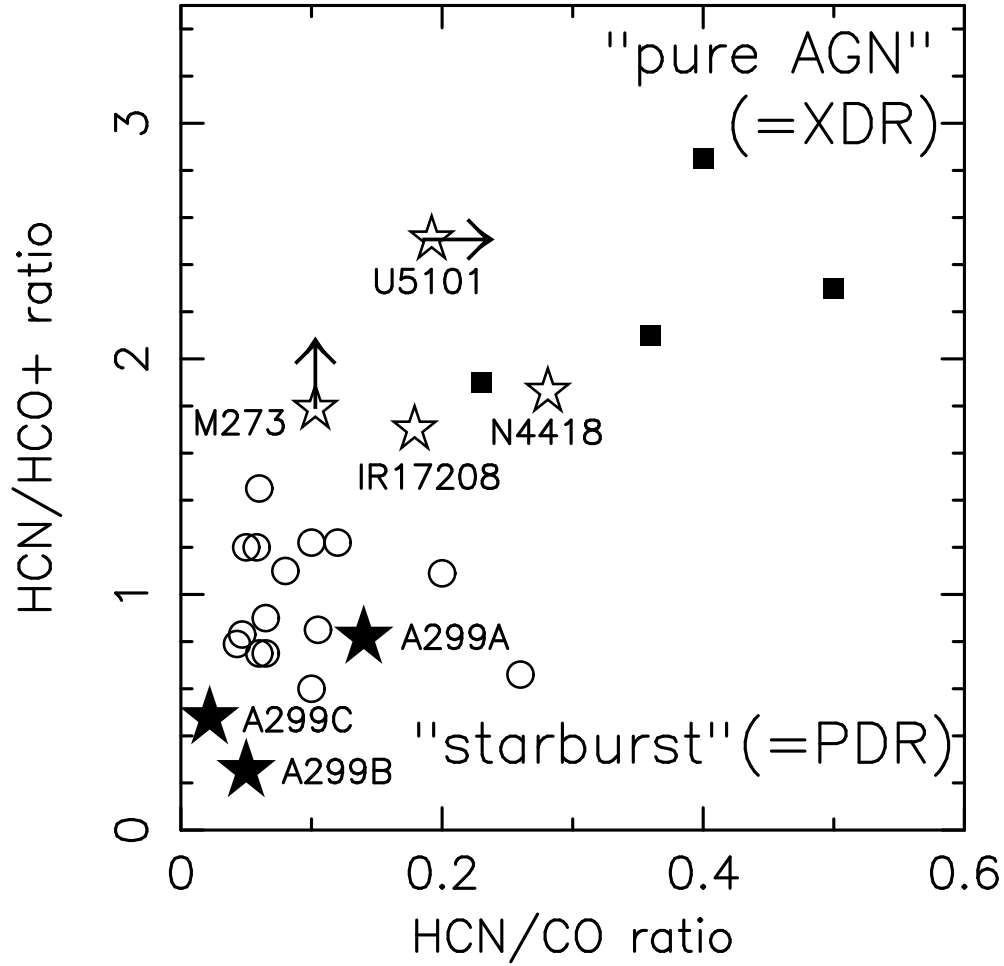


Fig. 8. HCN/HCO⁺ (ordinate) and HCN/CO (abscissa) ratios in brightness temperature ($\propto \lambda^2 \times \text{flux density}$). The three main merging components (A, B, and C) of Arp 299 are plotted as filled stars on the lower left side. No data point is plotted for Arp 299 C2 because CO data used for comparison are lacking at this exact location. Other LIRGs UGC 5101, Mrk 273, IRAS 17208–0014, and NGC 4418 (Imanishi et al. 2004; 2006b) are plotted as open stars. Other data points are taken from Kohno et al. (2001) and Kohno (2005), where sources with AGN-like (starburst-like) ratios are marked with filled squares (open circles). For all the plotted sources, HCN and HCO⁺ lines were observed simultaneously, using NMA. The beam patterns of HCN and HCO⁺ are virtually identical for each source, and so the same nuclear regions are probed. HCN and CO data were not taken simultaneously for all sources, so that their beam patterns are slightly different. However, this effect to our main discussions is expected to be small, given that HCN/HCO⁺ brightness-temperature ratios (not HCN/CO ratios) are primarily used (§4.3).